


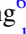










High-cadence Timing of Binary Pulsars with CHIME

Chia Min Tan^{1,2,3} , Emmanuel Fonseca^{4,5} , Kathryn Crowter⁶ , Fengqiu Adam Dong⁶ , Victoria M. Kaspi^{1,2} ,
Kiyoshi W. Masui^{7,8} , James W. McKee^{9,10} , Bradley W. Meyers³ , Scott M. Ransom¹¹ , and Ingrid H. Stairs⁶ 

¹ Department of Physics, McGill University, 3600 rue University, Montréal, QC H3A 2T8, Canada

² The Trottier Space Institute at McGill, 3550 rue University, Montréal, QC H3A 2A7, Canada

³ International Centre for Radio Astronomy Research, Curtin University, Bentley, WA 6102, Australia

⁴ Department of Physics and Astronomy, West Virginia University, Morgantown, WV 26506-6315, USA

⁵ Center for Gravitational Waves and Cosmology, Chestnut Ridge Research Building, Morgantown, WV 26505, USA

⁶ Department of Physics and Astronomy, University of British Columbia, 6224 Agricultural Road, Vancouver, BC V6T 1Z1, Canada

⁷ MIT Kavli Institute for Astrophysics and Space Research, Massachusetts Institute of Technology, 77 Massachusetts Avenue, Cambridge, MA 02139, USA

⁸ Department of Physics, Massachusetts Institute of Technology, 77 Massachusetts Avenue, Cambridge, MA 02139, USA

⁹ E.A. Milne Centre for Astrophysics, University of Hull, Cottingham Road, Kingston-upon-Hull, HU6 7RX, UK

¹⁰ Centre of Excellence for Data Science, Artificial Intelligence and Modelling (DAIM), University of Hull, Cottingham Road, Kingston-upon-Hull, HU6 7RX, UK

¹¹ National Radio Astronomy Observatory, 520 Edgemont Road, Charlottesville, VA 22903, USA

Received 2023 September 26; revised 2024 February 8; accepted 2024 February 9; published 2024 April 23

Abstract

We performed near-daily observations of the binary pulsars PSR J0218+4232, PSR J1518+4904, and PSR J2023+2853 with the Canadian Hydrogen Intensity Mapping Experiment (CHIME). For the first time, we detected the Shapiro time delay in all three pulsar binary systems, using only 2–4 yr of CHIME/Pulsar timing data. We measured the pulsar masses to be $1.49^{+0.23}_{-0.20} M_{\odot}$, $1.470^{+0.030}_{-0.034} M_{\odot}$, and $1.50^{+0.49}_{-0.38} M_{\odot}$, respectively. The companion mass to PSR J0218+4232 was found to be $0.179^{+0.018}_{-0.016} M_{\odot}$. We constrained the mass of the neutron star companion of PSR J1518+4904 to be $1.248^{+0.035}_{-0.029} M_{\odot}$, using the observed apsidal motion as a constraint on the mass estimation. The binary companion to PSR J2023+2853 was found to have a mass of $0.93^{+0.17}_{-0.14} M_{\odot}$; in the context of the near-circular orbit, this mass estimate suggests that the companion to PSR J2023+2853 is likely a high-mass white dwarf. By comparing the timing model obtained for PSR J0218+4232 with previous observations, we found a significant change in the observed orbital period of the system of $\dot{P}_b = 0.14(2) \times 10^{-12}$; we determined that this variation arises from “Shklovskii acceleration” due to the relative motion of the binary system, and used this measurement to estimate a distance of $d = (6.7 \pm 1.0)$ kpc to PSR J0218+4232. This work demonstrates the capability of high-cadence observations, enabled by the CHIME/Pulsar system, to detect and refine general-relativistic effects of binary pulsars over short observing timescales.

Unified Astronomy Thesaurus concepts: Pulsars (1306); Observational astronomy (1145); Interferometers (805)

1. Introduction

Timing studies of radio pulsars typically depend on the overall time span of observations to measure parameters that quantify apparent or intrinsic spin variations. Until recently, the cadence of pulsar-timing observations was limited to \sim monthly observing rates due to competitive telescope resources. The recent rise of high-cadence pulsar observing programs, such as the UTMOST (Jankowski et al. 2019; Lower et al. 2020) and Canadian Hydrogen Intensity Mapping Experiment (CHIME)/Pulsar (CHIME/Pulsar Collaboration et al. 2021) experiments, is producing uniquely dense data sets for a majority of the known pulsar population.

The CHIME/Pulsar system observes up to 10 sources simultaneously at any given time, allowing for near-daily observations of a selected set of pulsars. These circumstances have resulted in several studies that leverage high-cadence observations to make unique measurements of a growing number of sources. For example, high-cadence observations of the binary PSR J2108+4516 reveal extreme, intraday variations in the electromagnetic properties of the broadband pulsar signal due to a turbulent wind and/or circumstellar disk of its

high-mass companion star (Andersen et al. 2023). Moreover, high-cadence CHIME/Pulsar data recently contributed to the refined timing analysis of the binary PSR J0740+6620 for improved mass constraints (Fonseca et al. 2021), which directly led to the estimation of its radius using X-ray data obtained by the NICER telescope (Miller et al. 2021; Riley et al. 2021). High-cadence CHIME/Pulsar observations are supporting the analysis of pulsars discovered by the PALFA (Parent et al. 2022) and GBNCC (Stovall et al. 2014) surveys, as well as contributing to the data set developed by NANOGrav for improved detection of the nanohertz-frequency background of gravitational radiation (e.g., Lam 2018). In all of these aforementioned works, the high-cadence nature of the CHIME/Pulsar data affords new views of timing-based phenomena over observing timescales that cannot be achieved with other northern hemisphere instruments.

In this study, we perform high-precision timing analyses of three binary pulsars and explore the impact of high-cadence observations obtained with the CHIME/Pulsar backend. Two of these pulsars—PSRs J0218+4232 and J1518+4904—have long been known and well studied using archival data that span decades, and thus allow for independent checks of model accuracy. The remaining source, PSR J2023+2853, is a binary pulsar recently discovered in a survey of the Galactic plane using the Five-hundred Meter Aperture Synthesis Telescope (FAST; Han et al. 2021); to our knowledge, our study below

presents the first coherent timing solution of PSR J2023+2853 and demonstrates unambiguous period variations due to orbital motion. In Section 2, we outline the logistics of our observing program and processing of data. In Section 3, we outline the procedures used to construct timing models for all three binary pulsars. In Section 4, we present the results obtained from high-precision timing analyses.

2. Observations and Reduction

All data presented in this work were acquired with the CHIME telescope, a static interferometer that digitizes the sky as it drifts within its field of view (CHIME Collaboration et al. 2022). The CHIME telescope digitizes raw voltages from 1024 dual-polarization antennae, sensitive to the 400–800 MHz range, that are mounted on four half-cylinder reflectors that span an $80 \times 100 \text{ m}^2$ area; these digitized samples are then beamformed within the “FX” correlator to yield up to 10 baseband streams. Beamformed baseband data are phased to user-specified celestial positions in order to track the known radio sources.

These baseband streams are transmitted to the CHIME/Pulsar backend, a 10-node, real-time computing cluster that enables CHIME to make measurements of radio pulsars and other radio-transient phenomena under user-specified acquisition modes (CHIME/Pulsar Collaboration et al. 2021). Each CHIME/Pulsar node receives one baseband stream, complex-sampled at a rate of $2.56 \mu\text{s}$ and for 1024 frequency channels that span the 400–800 MHz range.

The timing data for our study were obtained using the CHIME/Pulsar backend in its “fold” mode. For all fold-mode observations, input voltages are coherently dedispersed (Hankins & Rickett 1975) and then folded using an existing timing model to average individual pulses into 10 s “subintegrations.” Coherent dedispersion is achieved by deconvolving the interstellar medium (ISM) impulse response function in the frequency domain from the input baseband prior to the detection and folding of the radio signal, which removes intrachannel smearing due to pulse dispersion (e.g., Hankins & Rickett 1975). We used the DSPSR software suite (van Straten & Bailes 2011) for real-time coherent dedispersion and folding, with a graphics processing unit mounted onto each CHIME/Pulsar node.

We initially took 10 observations of PSR J2023+2853 in filterbank mode with the CHIME/Pulsar backend, as no timing model that incorporates the binary orbital parameter existed at the time we began conducting our measurements. We folded the filterbank data to the spin period and dispersion measure (DM) presented in Han et al. (2021) and found that the apparent spin period of the pulsar changes between observations, indicating a potential binary companion. We modeled the variations in the apparent spin period, assuming that they arose from Doppler variations due to unmodeled orbital motion, and obtained an initial binary solution that describes a near-circular orbit with a binary period of 0.7 days and a projected semimajor axis of 4 lt-s. We then continued to observe PSR J2023+2853 in “fold” mode using a timing model that includes these orbital parameters.

The resultant fold-mode data yield time-averaged profiles for all four components of the Stokes polarization vector measured over 10 s subintegrations, a user-defined number of profile bins (n_{bin}), and 1024 frequency channels. We set the profile resolution to be $n_{\text{bin}} = 512$ for PSR J0218+4232, $n_{\text{bin}} = 1,024$ for PSR J1518+4904, and $n_{\text{bin}} = 256$ for PSR J2023+2853. In the case of PSR J0218+4232, its 2.3 ms spin period and the

fixed $2.56 \mu\text{s}$ baseband sample rate jointly lead to an upper limit in the allowed profile resolution, such that the largest binary value that can be used to evaluate Stokes profiles for fold-mode observations is 512. The profile resolution of PSR J2023+2853 is set at $n_{\text{bin}} = 256$, which is the default number set for any CHIME/Pulsar observation. By the time we decided to include PSR J2023+2853 in this work, there were approximately 1 yr of observations. Hence we decided to not change n_{bin} to keep the data set consistent.

2.1. Offline Excision and Reduction

During post-processing, we used the PSRCHIVE package (van Straten et al. 2012) and related utilities for offline cleaning and downsampling of raw timing data. We removed frequency channels that contain persistent radio frequency interference (RFI) using the fold-mode data cleaning tool CLFD (Morello et al. 2019), combined with a mask of frequency channels that produce unusable data for the particular day. These masks arise due to the variable unavailability of a small fraction of FX correlator nodes that each produce channelized time series for four frequency channels.

We further reduced the RFI-excised timing data by downsampling all spectra from 1024 frequency sub-bands to a smaller number, depending on the signal-to-noise ratio (S/N) of the pulsar, and fully integrating over time. We downsampled the number of frequency sub-bands to $n_{\text{sub}} = 32$ for PSR J0218+4232, $n_{\text{sub}} = 8$ for PSR J1518+4904, and $n_{\text{sub}} = 1$ for PSR J2023+2853. The frequency-resolved spectra of PSR J0218+4232 and PSR J1518+4904 provide opportunities for the modeling of dispersion variations, which we enact and discuss below.

2.2. Generation and Pruning of Times of Arrival

We used the common technique of cross-correlating Stokes I profiles with a noiseless “template” profile in the Fourier domain for determining the pulse times of arrival (TOAs) with high precision (Taylor 1992). Standard templates were generated by aligning and averaging at least 100 days of data using an adequate timing solution to form a single, representative profile for each pulsar considered in this work. These profiles were then fully averaged over all subintegrations and frequency channels and denoised using a wavelet-smoothing algorithm available in PSRCHIVE, PSRSMOOTH, to produce the standard templates.

As a final step in data preparation, we cleaned all TOA data sets using two common methods. First, we applied an S/N threshold to each TOA, such that a TOA derived from a Stokes I profile with $S/N < 4$ was discarded from the timing analysis presented below. Any remaining TOAs that significantly deviated from the timing model predictions—due to RFI and/or instrumental corruption whose statistics bypassed the S/N thresholds and RFI-cleaning algorithms—were manually removed. These TOA-cleaning steps removed 6.8%, 3.4%, and 10.7% of TOAs from the data sets for PSR J0218+4232, PSR J1518+4904, and PSR J2023+2853, respectively.

3. Timing Methods

An updated timing model based on CHIME/Pulsar data was produced for each pulsar through the weighted least-squares fitting of the TOAs produced (see Section 2.2) using the TEMPO¹² software package. For all timing models, we explored the

¹² <https://tempo.sourceforge.net>

significance of various astrophysical quantities: astrometric positions and their proper motion; spin frequency and its first derivative; the Keplerian binary parameters and their first-order variations; and the Shapiro delay parameters. The timing models include a temporal fit of the variation in the DM across the time span.

We also estimated ad hoc adjustment factors for our raw TOA uncertainties that produced reduced goodness-of-fit (χ^2) statistics of ~ 1 . These factors, commonly referred to as “EFAC” in the pulsar-timing literature, characterize the amount of increase in uncertainties needed for TOA residuals to exhibit Gaussian noise largely due to the imperfect estimation of the profile template shape (e.g., Agazie et al. 2023). We found that the EFAC values for our data sets varied from 1.2 to 1.25, indicating that the TOA estimation algorithm described in Section 2 largely determined the arrival times and their uncertainties in a robust manner. We did not further explore other separable sources of TOA noise (e.g., “ECORR”) for our sources, as such computational efforts are complicated by the large volumes of the CHIME/Pulsar data sets. As shown in Fonseca et al. (2021), the use of “wideband” TOA algorithms (e.g., Pennucci et al. 2014) can reduce the TOA volume by over an order of magnitude and will therefore be crucial for an efficient analysis of noise properties, though we reserve such an effort for future work.

3.1. Models for Orbital Motion

We used the ELL1 model (Lange et al. 2001) to describe the near-circular orbital motion of PSR J0218+4232 and PSR J2023+2853. For PSR J1518+4904, we used the DD and DDGR models (Damour & Deruelle 1985, 1986) to parameterize the periodic and secular orbital variations due to strong-field gravitation in terms of the mass of the companion star (m_c) and the total system mass ($m_{\text{tot}} = m_p + m_c$, where m_p is the mass of the pulsar).

Both the DDGR and ELL1 models characterize the Keplerian orbits in terms of the orbital period (P_b) and radial projection of the semimajor axis along the line of sight ($x = a \sin i/c$, where i is the orbital inclination angle), though they differ in their treatment of the orbital shape; the DDGR model uses the orbital eccentricity (e), the argument of periastron (ω), and the epoch of periastron passage (T_0) to describe the ellipticity, while the ELL1 model instead uses the “Laplace–Lagrange” parameters (ϵ_1 , ϵ_2) and the epoch of passage through the ascending-node longitude (T_{asc}) to describe the $O(e)$ deviations from circular orbits. The ELL1 eccentricity parameters are related in the following manner:

$$e = \sqrt{\epsilon_1^2 + \epsilon_2^2}, \quad (1)$$

$$\omega = \tan^{-1} \left(\frac{\epsilon_1}{\epsilon_2} \right), \quad (2)$$

$$T_0 = T_{\text{asc}} + \left(\frac{\omega}{2\pi} \right) P_b. \quad (3)$$

In practice, the ELL1 model is most applicable for binary pulsars with timing precision and orbital parameters that mutually satisfy the criterion $\sigma_{\text{TOA, rms}} > xe^2$, where xe^2 is the amplitude of the $O(e^2)$ correction to the ELL1 model.

Some binary pulsars eventually exhibit deviations from Keplerian motion due to various particularly extreme properties. Given the short timescale of our observations, the most

likely source of “post-Keplerian” (PK) variations is strong-field gravitation, which gives rise to apsidal motion ($\dot{\omega}$), orbital decay (\dot{P}_b), time dilation and gravitational redshift (γ), and the “range” (r) and “shape” (s) of the Shapiro delay. According to general relativity, these PK effects are functions of the mass and geometric information of the binary system (e.g., Damour & Taylor 1992):

$$\dot{\omega} = 3 \left(\frac{P_b}{2\pi} \right)^{-5/3} \frac{(T_\odot m_{\text{tot}})^{2/3}}{1 - e^2}, \quad (4)$$

$$\begin{aligned} \dot{P}_b = & -\frac{192\pi}{5} \left(\frac{P_b}{2\pi} \right)^{-5/3} \frac{T_\odot^{5/3} m_p m_c}{m_{\text{tot}}^{1/3} (1 - e^2)^{7/2}} \\ & \times \left(1 + \frac{73}{24} e^2 + \frac{37}{96} e^4 \right), \end{aligned} \quad (5)$$

$$\gamma = e \left(\frac{P_b}{2\pi} \right)^{1/3} T_\odot^{2/3} \frac{m_c (m_{\text{tot}} + m_c)}{m_{\text{tot}}^{4/3}}, \quad (6)$$

$$r = T_\odot m_c, \quad (7)$$

$$s \equiv \sin i = x \left(\frac{P_b}{2\pi} \right)^{-2/3} \frac{m_{\text{tot}}^{2/3}}{T_\odot^{1/3} m_c}, \quad (8)$$

where $T_\odot = GM_\odot/c^3 = 4.925490947 \mu\text{s}$ converts the masses to possess units of solar mass. The DD model directly measures the left-hand sides of Equations (4)–(8) in a theory-independent manner, while the DDGR model assumes Equations (4)–(8) directly measure m_c and m_{tot} .

3.2. Methods for Modeling ISM Variations

We modeled the DM variation of each pulsar using the DMX routine of TEMPO, which estimates a “local” value of the DM within contiguous, nonoverlapping time bins that span each data set. The measured DMs over different epochs are then subtracted from the residuals to model the other parameters. For PSR J0218+4232, we set the width of each DMX time bin to be no larger than 5 days; for PSR J1518+4904, we set the width of the DMX time bin to be no larger than 7 days; and for PSR J2023+2853, we set the DMX width to be no larger than 10 days. These widths were selected based on the variations in the observed trends, but were otherwise chosen arbitrarily.

We did not explicitly model or estimate the presence of pulse scatter broadening in any of the three pulsars subject to our study. This choice was made for two reasons: the use of TEMPO and channelized TOAs does not allow for simultaneous estimation of the DM and scattering timescale parameters; and there is a lack of a scatter-broadening signature in their CHIME/Pulsar data sets that is distinct from intrinsic profile evolution across the CHIME band. We nonetheless implicitly modeled the composite effects of scattering broadening and intrinsic profile evolution by fitting for “frequency-dependent” (FD) variations in our channelized TOAs. These variations were modeled using the FD time delay $\Delta t_{\text{FD}} = \sum_i c_i \ln^i \nu$, where c_i is the FD coefficient and ν is the electromagnetic frequency (NANOGrav Collaboration et al. 2015).

When simultaneously estimated with all other timing parameters with TEMPO, we found that at least one FD coefficient was sufficient for PSR J0218+4232 and the other two pulsars yielded insignificant FD parameters. Only two FD coefficients appear to be statistically significant for PSR J0218+4232, but the use of two coefficients leads to clear

degeneracy with the DMX parameters. This degeneracy likely arises due to several eras of intraday variations in the DM not being robustly modeled using our 5 days DMX bin widths. We therefore used only one FD coefficient in our final timing model for PSR J0218+4232 and manually estimated an EFAC using this “DMX+FD” timing model in order to correct our TOA uncertainties. The resultant EFAC value estimated from this model likely includes systematic biases from DM misestimation and any measurable variations in scatter broadening, both of which cannot be modeled by the c_i parameters, as they are presumed to be constant across each data set. However, the EFAC for PSR J0218+4232 is only $\sim 25\%$ larger than unity, indicating that the ISM variations are largely captured by the DMX+FD timing model.

DMX measurements are useful for evaluating ISM fluctuations across a wide range of length scales, and are often required for any analysis of submicrosecond timing effects like the Shapiro delay and nanohertz-frequency gravitational radiation (Jones et al. 2017; Valentina Sosa Fiscella et al. 2023). The DM variations observed in PSR J0218+4232 are particularly well resolved, as shown in Figure 1, such that a lack of DMX evaluation would contribute substantial “red” noise to our timing measurements and dominate the best-fit uncertainties. We reserve an analysis of the DMX time series for PSR J0218+4232 and other sources for a forthcoming census of low-frequency DM measurements with CHIME/Pulsar (J. W. McKee et al., in preparation).

3.3. Goodness-of-fit Grids of Shapiro Delay Parameters

With the timing model in hand, we used the Bayesian χ^2 gridding method developed by Splaver et al. (2002) to better determine the statistics of the Shapiro delay parameters for each pulsar. In this method, we iterated over the Shapiro delay parameters in a 100×100 grid of $(m_c, \cos i)$ values. At each $(m_c, \cos i)$ grid point, the timing model of each pulsar is refitted while fixing the values of the Shapiro delay parameters. A 2D probability density function (PDF), $p(m_c, \cos i | \text{data})$, is then generated by comparing the reduced χ^2 values obtained at different Shapiro delay parameter value pairs.

The 2D PDFs obtained for each pulsar were then used to constrain the Shapiro delay parameters and the mass of the pulsar. For the estimates of m_p , we used the Keplerian mass function (m_f), where

$$m_f = \frac{(m_c \sin i)^3}{m_{\text{tot}}^2} = \frac{4\pi^2 x^3}{T_\odot P_b^2}, \quad (9)$$

in order to enact the transformation in PDF variables:

$$p(m_c | \text{data}) = \int_0^\infty p(m_c, \cos i | \text{data}) d(\cos i), \quad (10)$$

$$p(m_p | \text{data}) = \int_0^\infty \int_0^\infty p(m_c, \cos i | \text{data}) \delta(\Delta m_p) d(\cos i) d(m_c), \quad (11)$$

$$p(\cos i | \text{data}) = \int_0^\infty p(m_c, \cos i | \text{data}) d(m_c), \quad (12)$$

where $\delta(x)$ is the Dirac delta function and $\Delta m_p = m_p - (\sqrt{(m_c \sin i)^3 / m_f} - m_c)$. We computed the cumulative distribution functions for each of the three above parameters to derive the median, 68.3%, and 95.4% credible interval values

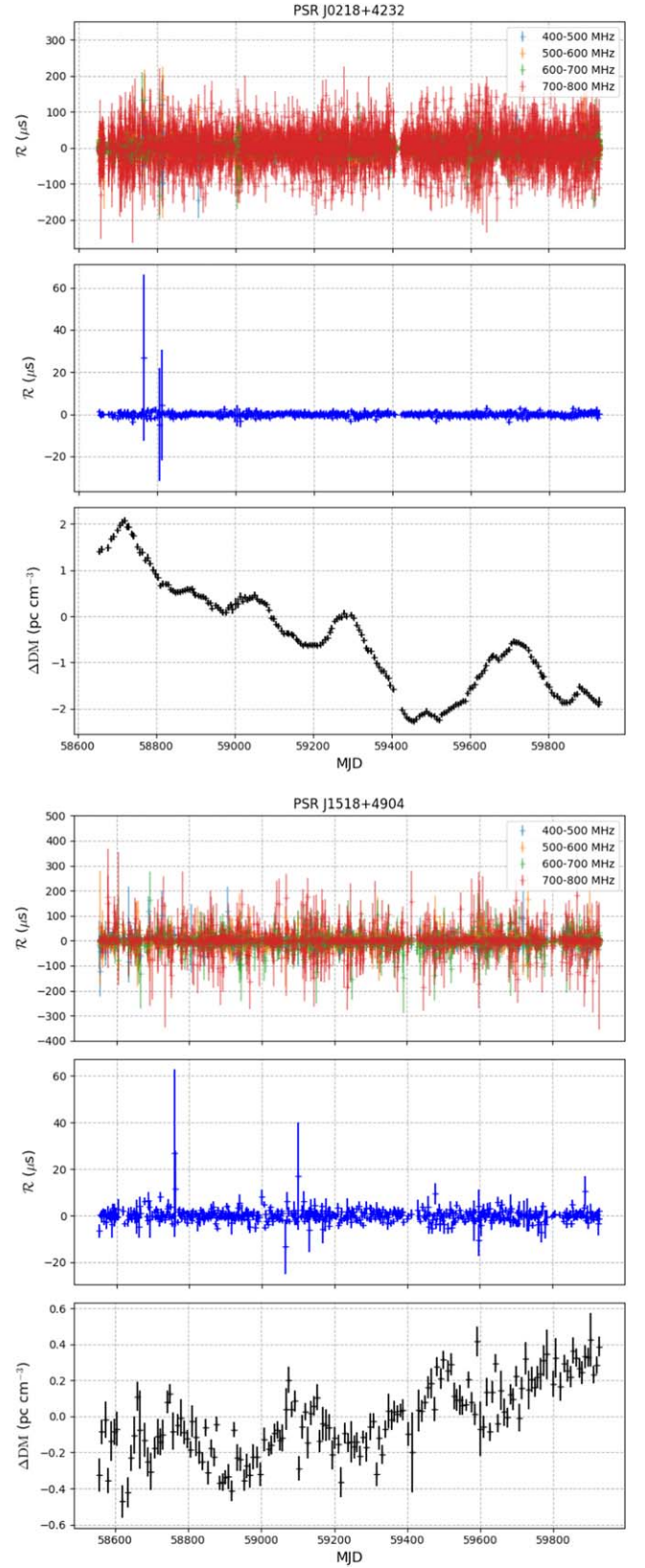


Figure 1. Frequency-resolved and frequency-averaged timing residuals (top and middle panels, respectively) and DM variation (bottom panels) of PSR J0218+4232 and PSR J1518+4904 over the observing span, as measured using the DMX method. While there is evidence for an annual variation in the DM of PSR J1518+4904, the ecliptic latitude of PSR J1518+4904, $\beta = 63^\circ$, is too large for electron density variations from the Sun to appear prominently in our DM time series.

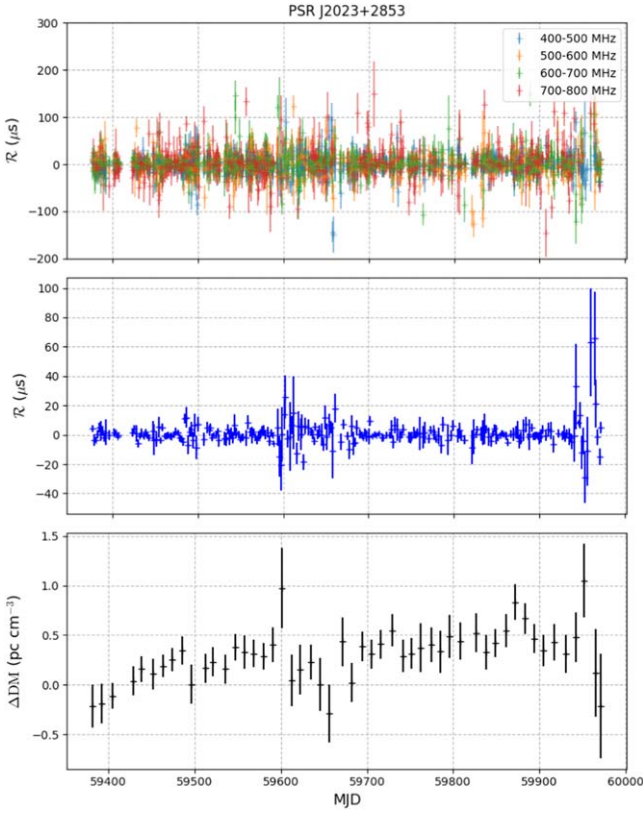


Figure 2. Frequency-resolved and frequency-averaged timing residuals (top and middle panels, respectively) and DM variation (bottom panel) of PSR J2023+2853 over the observing span, as measured using the DMX method.

for robust estimates of the relativistic parameters and their statistical uncertainties.

3.4. Constrained Shapiro Delay Grid for PSR J1518+4904

PSR J1518+4904 exhibits apsidal motion that has long been known to be consistent with the predictions of general relativity (Nice et al. 1996; Janssen et al. 2008), as given in Equation (4). Since $\dot{\omega}$ is a function of m_{tot} , its statistical significance can be used as a weight on grid-based estimates of $(m_c, \cos i)$ and can further delimit regions of preferred values, as has been done for other high-eccentricity systems. We therefore performed an additional χ^2 grid calculation for the CHIME/Pulsar timing data of PSR J1518+4904, where, at each grid point, we held values of m_c , m_{tot} , and $\dot{\omega}$ fixed, using Equation (9) to compute and fix $\sin i$.

We chose to perform grid calculations for PSR J1518+4904 in the (m_c, m_{tot}) phase space due to the high statistical significance of $\dot{\omega}$. After extensive analysis, we found that a grid over the (m_c, m_{tot}) phase space produces better constraints on the probability densities compared with that from the traditional $(m_c, \cos i)$ space. These calculations ultimately produced a map of probability density $p(m_c, m_{\text{tot}}|\text{data})$. Using this map, we derived estimates of the Shapiro delay parameters by marginalizing over the appropriate coordinate axes:

$$p(m_c|\text{data}) = \int_0^\infty p(m_c, m_{\text{tot}}|\text{data}) \delta(\Delta\dot{\omega}) d(m_{\text{tot}}), \quad (13)$$

$$p(m_p|\text{data}) = \int_0^\infty \int_0^\infty p(m_c, m_{\text{tot}}|\text{data}) \times \delta(\Delta m_p) d(m_{\text{tot}}) d(m_c), \quad (14)$$

$$p(\cos i|\text{data}) = \int_0^\infty \int_0^\infty p(m_c, m_{\text{tot}}|\text{data}) \times \delta(\Delta \cos i) d(m_{\text{tot}}) d(m_c), \quad (15)$$

where $\Delta \cos i = \cos i - \sqrt{1 - (m_f m_{\text{tot}}^2 / m_c^3)^{2/3}}$.

4. Results and Discussion

We obtained best-fit timing models for all three binary pulsars using TEMPO and the methods described in Section 3. The best-fit timing residuals and available DMX data for all binary pulsars are presented in Figures 1 and 2. A summary of each timing model, the derived parameters, and the best-fit statistics is presented in Table 1, while fixing the Shapiro delay values to the median values obtained from the χ^2 grids described in Section 3.3. The probability density maps of Shapiro-delay parameters for the three pulsars are shown in Figure 3. The constrained probability density of the neutron star masses in the PSR J1518+4904 system is shown in Figure 4.

4.1. New Shapiro Delay Measurements

For the first time, we detected the Shapiro time delay in all three binary pulsar systems. The near-daily observing cadence has clearly led to desirable coverage of the orbital phase over a 2–3 yr timescale; the lack of detection in prior work on PSRs J0218+4232 (Navarro et al. 1995; Desvignes et al. 2016; Perera et al. 2019) and J1518+4904 (Janssen et al. 2008) was likely impacted by low-density orbital phase coverage, despite their several-decade time span.

We consider the Shapiro delay in PSR J1518+4904 to be detected, since the total degeneracy of the $(m_c, \cos i)$ parameters—regions where the probability density is nonzero as $\cos i$ tends to unity—is statistically disfavored within the range of plausible companion mass values. However, the Shapiro delay in the PSR J1518+4904 system is nonetheless weakly detected, as the marginalized constraints on m_c and $\cos i$ produce a weak constraint on m_p . As a standalone effect, the current Shapiro delay in PSR J1518+4904 therefore offers no meaningful constraining power to the mass and geometry of the binary system, other than to restrict likely values of i . However, the use of $\dot{\omega}$ as a statistical weight in the χ^2 grid calculation leads to substantial improvements in the constraints of the physical parameters. We found that $m_p = 1.470_{-0.034}^{+0.030} M_\odot$ and $m_c = 1.248_{-0.029}^{+0.035} M_\odot$ (68.3% credibility), under the assumption that general relativity describes the observed apsidal motion.

Our estimates of m_p for PSRs J0218+4232 and J2023+2853— $m_p = 1.48_{-0.20}^{+0.24} M_\odot$ and $m_p = 1.42_{-0.32}^{+0.40} M_\odot$, respectively—are broadly consistent with values observed for the recycled pulsar population, though additional observations will further strengthen the constraints for delineating whether these pulsars lie on the high end of the neutron star mass spectrum. The estimates of the neutron star masses found in the PSR J1518+4904 system are consistent with the masses found in other DNS systems (e.g., Schwab et al. 2010).

Table 1
Best-fit Parameters and Derived Quantities for Binary Millisecond Pulsars

Global Parameters			
Pulsar name	PSR J0218+4232	PSR J1518+4904	PSR J2023+2853
Reference epoch (MJD)	58917	59134.411	59674
Observing time span (MJD)	58652–59930	58552–59929	59376–59930
Solar system planetary ephemeris	DE440	DE440	DE440
Binary model	ELL1	DDGR	ELL1
Clock standard	TT(BIPM2021)	TT(BIPM2021)	TT(BIPM2021)
Number of sub-bands	32	8	8
Width of DMX time bin (days)	5	7	10
TOA uncertainty adjustment factor (EFAC)	1.2	1.25	1.25
Timing Solution and Best-fit Metrics			
Right ascension (J2000), α (h:m:s)	02:18:06.362483(15)	15:18:16.797784(12)	20:23:21.06320(7)
decl. (J2000), δ (d:m:s)	42:32:17.3417(3)	49:04:34.08325(12)	28:53:41.4423(7)
Proper motion in right ascension, $\mu_\alpha \cos \delta$ (mas yr ⁻¹)	5.39(11)	-0.72(12)	-2.6(19)
Proper motion in decl., μ_δ (mas yr ⁻¹)	1.4(2)	-8.57(11)	-6(4)
Parallax, ϖ (mas)	...	4(2)	...
Pulse frequency, ν (s ⁻¹)	430.461056366647(6)	24.4289797496997(2)	88.269785050593(8)
First pulse frequency derivative, $\dot{\nu}$ (10 ⁻¹⁵ s ⁻²)	-14.34202(16)	-0.016197(10)	-0.212(3)
DM (pc cm ⁻³)	61.233749	11.611711	22.75
Orbital period, P_b (days)	2.02884608487(5)	8.63400496116(15)	0.71823040745(4)
Projected semimajor axis, x (lt-s)	1.98443196(5)	20.03942440(11)	4.0022194(4)
Epoch of periastron passage, T_0 (MJD)	...	59125.99829199(5)	...
Orbital eccentricity, e	...	0.249484383(9)	...
Longitude of periastron, ω (deg)	...	342.745426(2)	...
Epoch of ascending-node passage, T_{ASC} (MJD)	58915.445027883(14)	...	59390.14830429(2)
First Laplace–Lagrange parameter, ϵ_1 (10 ⁻⁵)	0.39(2)	...	1.11(2)
Second Laplace–Lagrange parameter, ϵ_2 (10 ⁻⁵)	0.50(2)	...	0.73(2)
First-order FD variation in channelized TOAs	-1.54(15) × 10 ⁻⁵
Number of TOAs	29889	7412	2623
χ^2	30192.25	7458.33	2690.70
Degrees of freedom	29675	7241	2560
Reduced χ^2	1.02	1.03	1.05
rms timing residual (μ s)	6.458	4.906	12.395
Gridded Estimates of the Masses and Orbital Inclination			
Mass of the companion, m_c (M_\odot)	0.179 ^{+0.018} _{-0.016}	1.248 ^{+0.035} _{-0.029}	0.93 ^{+0.17} _{-0.14}
Total mass of the system, m_{tot} (M_\odot)	...	2.7186(7)	...
Cosine of the inclination angle, $\cos i$	0.086 ^{+0.020} _{-0.018}	...	0.123 ^{+0.036} _{-0.032}
Derived Quantities			
Mass function, m_f (M_\odot)	0.0020384176(2)	0.115908122(2)	0.13343133(4)
Mass of the pulsar, m_p (M_\odot)	1.49 ^{+0.23} _{-0.20}	1.470 ^{+0.030} _{-0.038}	1.50 ^{+0.49} _{-0.38}
Inclination angle of the binary system, i , (deg)	85.1 ^{+1.0} _{-1.2}	49.6 ^{+1.6} _{-1.8}	83.0 ^{+1.8} _{-2.0}
Rate of advance of periastron, $\dot{\omega}$ (deg yr ⁻¹)	...	0.011373(2)	...
Time dilation and gravitational redshift parameter, γ	...	0.00463 ^{+0.00017} _{-0.00014}	...
Relativistic orbital decay, \dot{P}_b (10 ⁻¹²)	...	-0.001176(5)	...

4.2. Discussion of Individual Sources

4.2.1. PSR J0218+4232

The properties of the PSR J0218+4232 system, first discovered by Navarro et al. (1995), were most recently modeled by Desvignes et al. (2016) and later Perera et al. (2019), as part of the International Pulsar Timing Array (IPTA) project. No apparent detection of the Shapiro delay was made in either of their extended data sets. By contrast, we were able to successfully detect the Shapiro delay signature in the PSR J0218+4232 system, due to the near-daily cadence of our CHIME/Pulsar data set. The measurement of $\cos i$ is consistent with the constraints placed on the orbital geometry and spin orientation of PSR J0218+4232 derived from low-frequency

polarimetry (Stairs et al. 1999), and suggests that the misalignment between the axes of orbital angular momentum and pulsar spin is nearly orthogonal.

The statistical significance of the Shapiro delay remains high even when incorporating hundreds of degrees of freedom from the DMX model into our timing analysis. However, when included as a free parameter, the best-fit measured proper motion in decl. was found to be inconsistent with the measurements by both Desvignes et al. (2016) and Perera et al. (2019), as well as a Very Long Baseline Interferometry (VLBI) measurement by Du et al. (2014), both in magnitude and sign. Moreover, we found that fits of the timing signature due to parallax yielded negative values with apparent statistical significance. We remodeled the properties of PSR J0218+4232

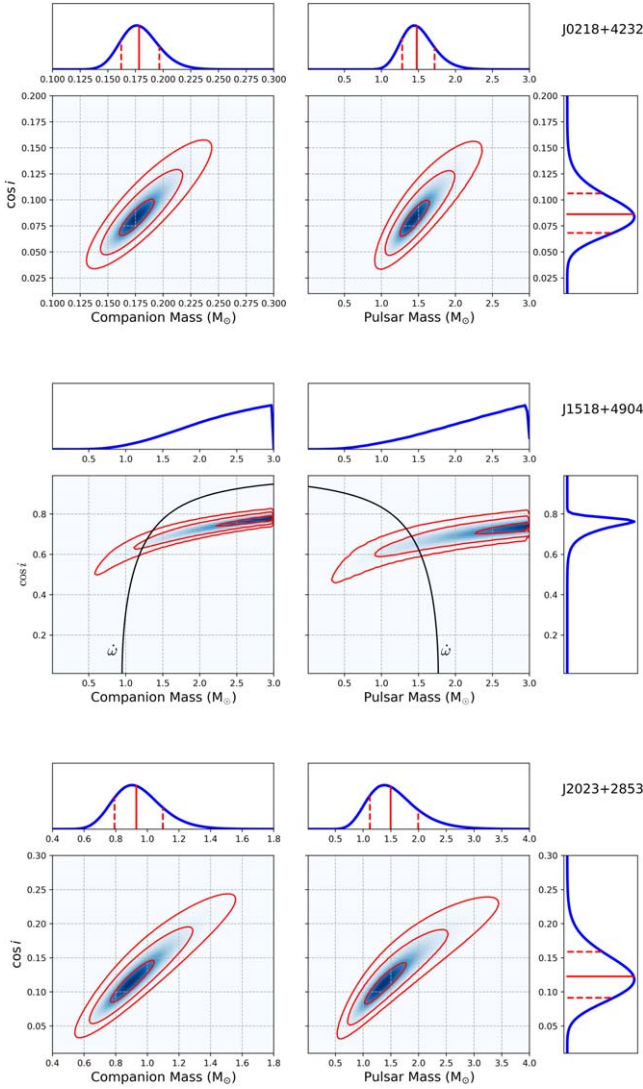


Figure 3. The probability density maps of Shapiro delay parameters for PSRs J0218+4232, J1518+4904, and J2023+2853. The red contours of each map represent regions of probability that contain 68.3%, 95.4%, and 99.3% credibility, respectively. In the outer panels, the red solid lines denote median values, while the red dashed lines represent 68.3% credible intervals. For PSR J1518+4904, the black curves of each map represent the range of allowed masses inferred by the observed $\dot{\omega}$ when assuming that general relativity describes the apsidal motion; the precision in our measurement of $\dot{\omega}$ is so high that the two curves appear as a single line on each map. No credible intervals are presented in the outer panels for PSR J1518+4904, as the majority of the probability density is not fully encapsulated in the map bounds.

after fixing the parallax to zero and the proper motion to the model-independent values determined by Du et al. (2014) of $\mu_\alpha \cos \delta = 5.35 \text{ mas yr}^{-1}$ and $\mu_\delta = -3.74 \text{ mas yr}^{-1}$, and found that the best-fit DM variations of the pulsar changed significantly. We suspect that these discrepancies arise due to several reasons: the sensitivity of our data set on PSR J0218+4232 to intraday DM variations; our observations being scheduled such that the pulsar is observed at the same local sidereal time every day; and that the binary orbit of PSR J0218+4232 is slightly more than exactly 2 days, resulting in the variation of the orbital Doppler shift being absorbed into the DM variation modeling. This apparent DM variation is found to be degenerate with the astrometric parameters and manifests itself as an offset to the measured proper motion in decl. These issues do not arise with the other pulsars analyzed in our study.

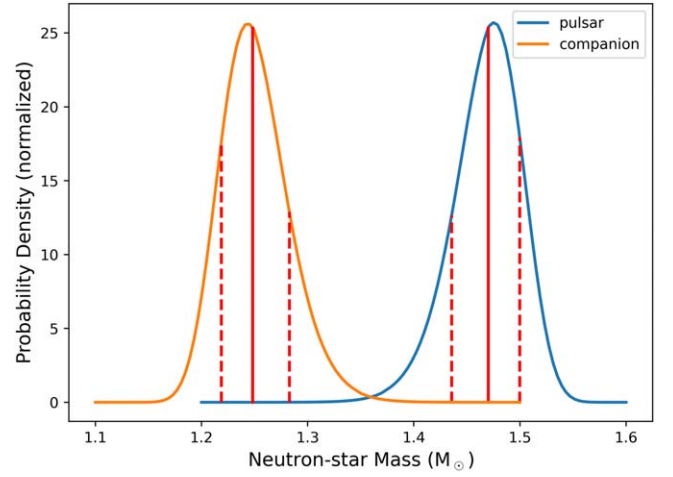


Figure 4. The constrained probability density of the neutron star masses in the PSR J1518+4904 system, derived from posterior PDFs of the Shapiro delay parameters computed while using the observed apsidal motion as a constraint on the likelihood function. The red solid line is the median value, while the red dashed lines represent 68.3% credible intervals of the masses.

We nonetheless found that the difference in the proper motion used to model the binary system resulted in an insignificant difference in the measured Shapiro delay parameters. We found $m_c = 0.182^{+0.019}_{-0.017} M_\odot$ and $\cos i = 0.0911^{+0.020}_{-0.019}$ after fixing the proper motion of the system to be the values obtained by Du et al. (2014). These values remain consistent at the 68.3% credibility level with values derived from a timing model that sets the proper motion of the system as free parameters.

The CHIME/Pulsar timing model provides a high-cadence snapshot of the PSR J0218+4232 orbit that may have evolved over the decades since its discovery. We therefore compared our values of the orbital elements with those most recently published for the second data release of the IPTA (Perera et al. 2019); the IPTA data set for PSR J0218+4232 spans ~ 17.5 yr and consists of TOAs collected with a variety of European observatories. As the timing model from Perera et al. (2019) does not include any Shapiro delay modeling, we first downloaded the publicly available data from their work and refit the release model for PSR J0218+4232 after incorporating the Shapiro delay parameters as degrees of freedom. This refitting was done to ensure robust comparisons of models and to avoid potential biasing of orbital parameters due to the presence of an unmodeled Shapiro delay (Freire & Wex 2010).

Using this new IPTA model, we found that x has remained the same between the two orbital models to within 1σ , where σ is the larger of the two statistical uncertainties in the fit parameter. We inferred an approximate rate of change in x to be $\dot{x} \approx \Delta x / \Delta T_{\text{asc}} = -5(4) \times 10^{-15} \text{ s s}^{-1}$. This limit on \dot{x} is consistent with the maximum value of \dot{x} due to the changing of orientation due to proper motion: given our estimate of i and that $(\dot{x})_{\text{max}} = x\mu |\cot i|$ (Nice et al. 2001), we found that $|\dot{x}|_{\text{max}} \sim 10^{-16} \text{ s s}^{-1}$.

By contrast, we found that there is a significant change in P_b between our CHIME/Pulsar timing model and the Shapiro-delay-incorporated model derived from the IPTA data set from Perera et al. (2019). We computed the change in P_b between the two epochs to be $\dot{P}_b \approx \Delta P_b / \Delta T_{\text{asc}} = 0.14(2) \times 10^{-12}$, where the uncertainty is dominated by those estimated for P_b .

The fact that \dot{P}_b is positive suggests this variation is not dominated by decay due to the emission of gravitational waves from the system. Instead, this rate of change most likely arises from variations in the Doppler shift due the relative motion between PSR J0218+4232 and Earth. This motion results in contributions of \dot{P}_b to the total, observed value, such that $(\dot{P}_b)_{\text{obs}} = (\dot{P}_b)_{\text{GR}} + (\dot{P}_b)_{\text{DR}} + (\dot{P}_b)_z + (\dot{P}_b)_\mu$, where $(\dot{P}_b)_{\text{GR}}$ is the general-relativistic orbital decay rate presented in Equation (5) and the additional terms are defined as follows (Shklovskii 1970; Kuijken & Gilmore 1989; Damour & Taylor 1992; Nice et al. 1996):

$$(\dot{P}_b)_{\text{DR}} = -P_b \cos b \left(\frac{\Theta_0^2}{cR_0} \right) \left(\cos l + \frac{\kappa^2}{\sin^2 l + \kappa^2} \right), \quad (16)$$

$$(\dot{P}_b)_z = -1.08 \times 10^{-19} \frac{P_b}{c} \times \left(\frac{1.25z}{[z^2 + 0.0324]^{1/2}} + 0.58z \right) \sin b, \quad (17)$$

$$(\dot{P}_b)_\mu = \frac{\mu^2 d}{c} P_b. \quad (18)$$

The various terms in Equations (16)–(18) are defined as follows: b and l are the Galactic latitude and longitude, respectively; Θ_0 and R_0 are the Galactocentric circular speed and distance parameters for the solar system barycenter, respectively; $\kappa = (d/R_0)\cos b - \cos l$, where d is the distance to the pulsar; $z = d \sin b$ is the projected vertical distance of the pulsar binary system from the Galactic plane; and $\mu = \sqrt{\mu_\alpha^2 + \mu_\delta^2}$ is the magnitude of proper motion. We assumed $\Theta_0 = 236.9(4.2)$ km s⁻¹ and $R_0 = 8.178(26)$ kpc, as recently determined by Gravity Collaboration et al. (2019).

By modeling $(\dot{P}_b)_{\text{obs}}$ in terms of Equations (5) and (16)–(18), we found that large values of d are needed to produce our derived value. We performed a Monte Carlo analysis of d by randomly sampling the $\{m_p, m_c, \Theta_0, R_0, \mu, (\dot{P}_b)_{\text{obs}}\}$ parameters, based on their best available uncertainties, which we assumed to be Gaussian,¹³ and by computing d using Equations (5) and (16)–(18) for each combination of parameter values. Our estimate of $(\dot{P}_b)_{\text{obs}}$ from this Monte Carlo analysis corresponds to $d = (6.7 \pm 1.0)$ kpc, where the statistics reflect the mean and standard deviation of the resultant distribution in d . This distance is statistically consistent with the VLBI distance determined by Du et al. (2014), $d = 6.3$ kpc, where the combined effects give a predicted estimate of $\dot{P}_b \approx 0.12 \times 10^{-12}$ for this large distance. Conversely, a distance to the pulsar of $d = 3.15$ kpc, as suggested by Verbiest & Lorimer (2014), would yield an expected $\dot{P}_b \approx 0.06 \times 10^{-12}$. This latter value of d is inconsistent with our estimate of $(\dot{P}_b)_{\text{obs}}$ at the 4σ level. Otherwise, the spectroscopic analysis of the white dwarf companion (Bassa et al. 2003) places the binary pulsar system at a distance of $d = 4$ kpc for a white dwarf model that is consistent with the measured mass. This gives an expected $\dot{P}_b \approx 0.08 \times 10^{-12}$, which differs by 3σ from our measured \dot{P}_b value.

While the difference between our measured \dot{P}_b value and the expected \dot{P}_b from several distance estimates is tantalizing, the

specific form of Equation (17) assumes a model of vertical acceleration due to the surface mass distribution of the Galactic disk estimated by Kuijken & Gilmore (1989). We separately utilized an alternative model of the Galactic surface mass density developed by Holmberg & Flynn (2000, 2004), which predicts that

$$(\dot{P}_b)_z = -[2.27|z|_{\text{kpc}} + 3.68(1 - \exp[-4.61|z|_{\text{kpc}}])] \times 10^{-11} \left(\frac{P_b |\sin b|}{c} \right) \quad (19)$$

and has been used in recent pulsar-timing analyses (e.g., Lazaridis et al. 2009; Zhu et al. 2015). Both Equations (17) and (19) predict that $(\dot{P}_b)_z \approx -10^{-14}$ s s⁻¹ for a distance range $3.15 < d < 6.3$ kpc, which is subdominant to the ‘‘Shklovskii acceleration’’ defined in Equation (18). The preference for a large distance to PSR J0218+4232 therefore remains, regardless of the choice of a model of $(\dot{P}_b)_z$. However, these models likely lose accuracy for large z ; further development of viable Galactic acceleration models (e.g., Chakrabarti et al. 2021) will therefore improve the robustness of our timing-based constraint on d for PSR J0218+4232.

4.2.2. PSR J1518+4904

The most recent analysis of the PSR J1518+4904 binary system was conducted by Janssen et al. (2008), using a data set that spanned over 12 yr. The properties obtained by Janssen et al. (2008) are broadly similar to the model we produced in our analysis of CHIME/Pulsar timing data. However, they did not meaningfully detect the Shapiro delay from their observations. Janssen et al. (2008) instead derived an upper limit on the inclination of the orbit at $i < 47^\circ$, based on their nondetection of the Shapiro delay. Using this constraint, they estimated the masses of the pulsar and companion to be $m_p < 1.17 M_\odot$ and $m_c > 1.55 M_\odot$.

In our work, we were able to significantly detect the signature of the Shapiro delay from PSR J1518+4904, with the grid-based inclination of the orbit estimated to be $i = 49.6_{-1.8}^{+1.6}$. The derived inclination angle is marginally higher than the upper limit placed by Janssen et al. (2008). The low inclination angle suggests that the Shapiro delay signature from the PSR J1518+4904 system is weak, and is only detectable due to a combination of the significant apsidal motion and high-cadence sampling of our data over a much shorter time span of less than 4 yr.

The measured masses of the PSR J1518+4904 system also show that the pulsar is the more massive object, with $m_p = 1.470_{-0.034}^{+0.030} M_\odot$, while the companion neutron star has a smaller mass of $m_p = 1.248_{-0.029}^{+0.035} M_\odot$. The rotational properties of the pulsar suggest that it is a partially recycled pulsar and would be the firstborn neutron star in the system. The firstborn neutron star being the heavier object in a double-neutron-star system is consistent with most others that are observed (See Özel & Freire 2016; Tauris et al. 2017 and references therein.) Tauris et al. (2017) studied the formation of such systems and suggested that the mass discrepancy between the neutron star is unlikely due to the accretion of mass by the firstborn neutron star, but rather due to the progenitor of the second neutron star being stripped of its mass more significantly due to the first neutron star prior to the second supernova.

¹³ While our Shapiro delay analysis shows that the posterior PDFs for m_p and m_c are non-Gaussian, the $(\dot{P}_b)_{\text{GR}}$ term is subdominant to all other sources of variation in P_b , which therefore has no bearing on our Monte Carlo estimate of d .

We compared our best-fit Keplerian elements with those published by Janssen et al. (2008), in order to detect or constrain variations between the two data sets. No significant changes in x or P_b beyond 2σ were found after accounting for clock-correction differences between the two timing solutions. The limits we derived from this analysis— $|x| < 3 \times 10^{-14}$ and $|\dot{P}_b| < 6 \times 10^{-12}$ —are consistent with those determined from the longer data set studied by Janssen et al. (2008).

The accuracy and precision in our measurement of $\dot{\omega}$ are nearly identical to the values published by Janssen et al. (2008). It is worth noting that this result arises from our analysis despite the CHIME/Pulsar data set being a factor of ~ 3.5 shorter in time span than that analyzed by Janssen et al. (2008). This circumstance demonstrates that the CHIME/Pulsar instrument can produce high-accuracy snapshots of pulsar orbits on much faster timescales than possible elsewhere, owing to the nearly daily cadence of our observations, and thus allows for the quickened resolution of orbital variations over time. As originally noted by Janssen et al. (2008), the statistical uncertainty in the observed apsidal motion is comparable in magnitude to variations that arise evolving the orientation of the binary system due to proper motion (e.g., Kopeikin 1996). We therefore consider our measured $\dot{\omega}$ to arise purely from general-relativistic orbital motion. A combination of the CHIME/Pulsar data set with that published by Janssen et al. (2008), which will lead to substantially improved measurement of $\dot{\omega}$ and likely other relativistic variations, will be the subject of future work.

4.2.3. PSR J2023+2853

PSR J2023+2853 is a pulsar recently discovered by the FAST Galactic Plane Pulsar Snapshot survey (Han et al. 2021). Han et al. (2021) noted that PSR J2023+2853 is detected with significant acceleration, suggesting that the pulsar has a binary companion. Our independent observations revealed that the pulsar is in a 0.7 days long orbit, with a detectable Shapiro delay signature that revealed a companion with $m_c = 0.90^{+0.14}_{-0.12} M_\odot$. Considering the low eccentricity of the orbit and the mass of the companion, it is likely to be a high-mass carbon–oxygen white dwarf.

The relatively long rotation period of PSR J2023+2853 ($P > 10$ ms) compared to typical millisecond pulsars, combined with the relatively heavy mass of the companion ($m_c > 0.5 M_\odot$), suggests that it is part of the class of binary system known as intermediate-mass binary pulsars (IMBPs; Camilo et al. 2001). IMBPs are thought to be formed from the accretion of a main-sequence companion of $4\text{--}8 M_\odot$, in which the pulsar itself is partially recycled. PSR J2023+2853 also has a larger eccentricity compared to typical pulsar binary systems of similar orbital period, as well as a low scale height of $0.13 < z < 0.17$ kpc, for an estimated distance to the pulsar of $1.6\text{--}2.0$ kpc, as predicted by the Galactic electron density models (Cordes & Lazio 2002; Yao et al. 2017). These properties are consistent with the system being an IMBP.

An optical source with $r = 23.55$, $g - r = 1.43$, SDSS J202320.88+285345.3, is found in the Sloan Digital Sky Survey (SDSS; York et al. 2000; Abduro'uf et al. 2022), around $5''$ from the timing position of PSR J2023+2853. However, the photometric properties of the source, specifically the SDSS $u - g$, $g - r$, and $r - i$ colors, are inconsistent with it being a white dwarf, using the white dwarf cooling model described by Bergeron et al. (1995), Holberg & Bergeron (2006), Kowalski & Saumon (2006),

Bergeron et al. (2011), Tremblay et al. (2011), Blouin et al. (2018), and Bédard et al. (2020),¹⁴ even considering the Galactic extinction along the line of sight, which gives $r = 24.17$, $g - r = 1.23$ (Schlegel et al. 1998; Schlafly & Finkbeiner 2011). This suggests that the optical source is not associated with PSR J2023+2853. No sources are detected within $5''$ of PSR J2023+2853 in the Two Micron All Sky Survey (Skrutskie et al. 2006) or the Gaia mission (Gaia Collaboration et al. 2016, 2022). The nondetection of the white dwarf companion is expected, as it should have an r -magnitude of 25 in SDSS, smaller than the detection threshold of the surveys above, based on the r -magnitude of the detection made on a similar white dwarf in another pulsar binary system, PSR J1658+3630 (Tan et al. 2020).

5. Conclusions

By leveraging the near-daily observations conducted by CHIME/Pulsar, we were able to, for the first time, model the Shapiro time delay of the binary pulsars PSRs J0218+4232, J1518+4904, and J2023+2853. In the case of J1518+4904, we assumed that the observed apsidal motion was described by general relativity, so that its significance could be used to constrain the component masses of the system. These measurements allowed us to constrain the masses of the pulsars in the binary systems to be $1.48^{+0.24}_{-0.20} M_\odot$, $1.470^{+0.030}_{-0.034} M_\odot$, and $1.50^{+0.49}_{-0.38} M_\odot$, respectively. The measured pulsar masses of all three systems are well within the known mass distribution of neutron stars (Özel & Freire 2016).

We were also able to measure the mass of the companion neutron star to PSR J1518+4904 to be $m_c = 1.248^{+0.035}_{-0.029} M_\odot$, and, for the first time, to model the binary properties of PSR J2023+2853, revealing a relatively high-mass companion of $m_c = 0.93^{+0.17}_{-0.14} M_\odot$. The measured mass, together with a near-circular orbit, suggest that the companion is likely a high-mass carbon–oxygen white dwarf, and that the system is an IMBP. The low mass of the companion to PSR J0218+4232, a helium white dwarf of $m_c = 0.179^{+0.019}_{-0.016} M_\odot$, is consistent with predictions from models of millisecond pulsar formation through long-term mass transfer within low-mass X-ray binary systems (e.g., Tauris & Savonije 1999).

We also obtained an estimate of the change in orbital period of PSR J0218+4232 between the epoch of the observations from Perera et al. (2019) and our observations. We found that the primary contribution to the orbital period change is due to variations in the Doppler shift from Shklovskii acceleration, and that the change corresponds to a distance to the pulsar of $d = (6.7 \pm 1.0)$ kpc, consistent with the measurement of $d = 6.3$ kpc from the VLBI observation conducted by Du et al. (2014). No significant changes were observed in the CHIME/Pulsar estimates of the orbital elements of PSR J1518+4904.

Our success in obtaining measurements of the masses of these pulsars through Shapiro delay modeling, using the near-daily observations from CHIME/Pulsar, has prompted us to observe other binary pulsar systems on a near-daily basis. These high-cadence observations will help constrain the masses of the objects in these systems in order to provide an even larger sample of pulsar masses and relativistic measurements. We also continue to observe the three pulsar binary systems in this study, in order to further constrain their properties.

¹⁴ <https://www.astro.umontreal.ca/~bergeron/CoolingModels/>

Future work on these sources will also investigate the DM variations and noise properties of the high-cadence CHIME/Pulsar data sets, which could slightly modify the precision of our mass and geometric measurements. Moreover, subsequent studies will compute and analyze “wideband” TOAs, in order to maximize the arrival time precision and reduce the TOA data volumes for efficient modeling of timing phenonema.

Acknowledgments

We acknowledge that CHIME is located on the traditional, ancestral, and unceded territory of the Syilx/Okanagan people. We thank Marten van Kerkwijk for valuable discussion.

We are grateful to the staff of the Dominion Radio Astrophysical Observatory, which is operated by the National Research Council of Canada. CHIME is funded by a grant from the Canada Foundation for Innovation (CFI) 2012 Leading Edge Fund (Project 31170) and by contributions from the provinces of British Columbia, Québec, and Ontario. The CHIME/FRB Project, which enabled development in common with the CHIME/Pulsar instrument, is funded by a grant from the CFI 2015 Innovation Fund (Project 33213), by contributions from the provinces of British Columbia and Québec, and by the Dunlap Institute for Astronomy and Astrophysics at the University of Toronto. Additional support was provided by the Canadian Institute for Advanced Research (CIFAR), McGill University and the McGill Space Institute thanks to the Trottier Family Foundation, and the University of British Columbia. The CHIME/Pulsar instrument hardware was funded by NSERC RTI-1 grant EQPEQ 458893-2014.

F.A.D. is supported by the UBC Four Year Fellowship. V. M.K. holds the Lorne Trottier Chair in Astrophysics & Cosmology, a Distinguished James McGill Professorship, and receives support from an NSERC Discovery grant (RGPIN 228738-13), from an R. Howard Webster Foundation Fellowship from CIFAR, and from the FRQNT CRAQ. K.W.M. holds the Adam J. Burgasser Chair in Astrophysics and is supported by NSF grants (2008031, 2018490). The National Radio Astronomy Observatory is a facility of the National Science Foundation operated under cooperative agreement by Associated Universities, Inc. S.M.R. is a CIFAR Fellow and is supported by the NSF Physics Frontiers Center award 2020265. Pulsar research at UBC is funded by an NSERC Discovery Grant and by the Canadian Institute for Advanced Research.

This research was enabled in part by support provided by the BC Digital Research Infrastructure Group and the Digital Research Alliance of Canada (<https://alliancecan.ca/>).

Software: DSPSR (van Straten & Bailes 2011), PSRDADA (<http://psrdada.sourceforge.net>), PSRCHIVE (Hotan et al. 2004; van Straten et al. 2012), PRESTO (<https://github.com/scottransom/presto>), TEMPO (<https://tempo.sourceforge.net>), TEMPO2 (Hobbs et al. 2006).

ORCID iDs

Chia Min Tan  <https://orcid.org/0000-0001-7509-0117>
 Emmanuel Fonseca  <https://orcid.org/0000-0001-8384-5049>
 Kathryn Crowter  <https://orcid.org/0000-0002-1529-5169>
 Fengqiu Adam Dong  <https://orcid.org/0000-0003-4098-5222>
 Victoria M. Kaspi  <https://orcid.org/0000-0001-9345-0307>
 Kiyoshi W. Masui  <https://orcid.org/0000-0002-4279-6946>
 James W. McKee  <https://orcid.org/0000-0002-2885-8485>

Bradley W. Meyers  <https://orcid.org/0000-0001-8845-1225>
 Scott M. Ransom  <https://orcid.org/0000-0001-5799-9714>
 Ingrid H. Stairs  <https://orcid.org/0000-0001-9784-8670>

References

- Abdurro'uf, Accetta, K., Aerts, C., et al. 2022, *ApJS*, 259, 35
 Agazie, G., Anumarlapudi, A., Archibald, A. M., et al. 2023, *ApJL*, 951, L10
 Andersen, B. C., Fonseca, E., McKee, J. W., et al. 2023, *ApJ*, 943, 57
 Bassa, C. G., van Kerkwijk, M. H., & Kulkarni, S. R. 2003, *A&A*, 403, 1067
 Bédard, A., Bergeron, P., Brassard, P., & Fontaine, G. 2020, *ApJ*, 901, 93
 Bergeron, P., Wesemael, F., & Beauchamp, A. 1995, *PASP*, 107, 1047
 Bergeron, P., Wesemael, F., Dufour, P., et al. 2011, *ApJ*, 737, 28
 Blouin, S., Dufour, P., & Allard, N. F. 2018, *ApJ*, 863, 184
 Camilo, F., Lyne, A. G., Manchester, R. N., et al. 2001, *ApJL*, 548, L187
 Chakrabarti, S., Chang, P., Lam, M. T., Vigeland, S. J., & Quillen, A. C. 2021, *ApJL*, 907, L26
 CHIME Collaboration, Amiri, M., Bandura, K., et al. 2022, *ApJS*, 261, 29
 CHIME/Pulsar Collaboration, Amiri, M., Bandura, K. M., et al. 2021, *ApJS*, 255, 5
 Cordes, J. M., & Lazio, T. J. W. 2002, arXiv:astro-ph/0207156
 Damour, T., & Deruelle, N. 1985, *AHPA*, 43, 107
 Damour, T., & Deruelle, N. 1986, *AHPA*, 44, 263
 Damour, T., & Taylor, J. H. 1992, *PhRvD*, 45, 1840
 Desvignes, G., Caballero, R. N., Lentati, L., et al. 2016, *MNRAS*, 458, 3341
 Du, Y., Yang, J., Campbell, R. M., et al. 2014, *ApJL*, 782, L38
 Fonseca, E., Cromartie, H. T., Pennucci, T. T., et al. 2021, *ApJL*, 915, L12
 Freire, P. C. C., & Wex, N. 2010, *MNRAS*, 409, 199
 Gaia Collaboration, Prusti, T., de Bruijne, J. H. J., et al. 2016, *A&A*, 595, A1
 Gaia Collaboration, Vallenari, A., Brown, A. G. A., et al. 2023, *A&A*, 674, A1
 Gravity Collaboration, Abuter, R., Amorim, A., et al. 2019, *A&A*, 625, L10
 Han, J. L., Wang, C., Wang, P. F., et al. 2021, *RAA*, 21, 107
 Hankins, T. H., & Rickett, B. J. 1975, *MComp*, 14, 55
 Hobbs, G. B., Edwards, R. T., & Manchester, R. N. 2006, *MNRAS*, 369, 655
 Holberg, J. B., & Bergeron, P. 2006, *AJ*, 132, 1221
 Holmberg, J., & Flynn, C. 2000, *MNRAS*, 313, 209
 Holmberg, J., & Flynn, C. 2004, *MNRAS*, 352, 440
 Hotan, A. W., van Straten, W., & Manchester, R. N. 2004, *PASA*, 21, 302
 Jankowski, F., Bailes, M., van Straten, W., et al. 2019, *MNRAS*, 484, 3691
 Janssen, G. H., Stappers, B. W., Kramer, M., et al. 2008, *A&A*, 490, 753
 Jones, M. L., McLaughlin, M. A., Lam, M. T., et al. 2017, *ApJ*, 841, 125
 Kopeikin, S. M. 1996, *ApJL*, 467, L93
 Kowalski, P. M., & Saumon, D. 2006, *ApJL*, 651, L137
 Kuijken, K., & Gilmore, G. 1989, *MNRAS*, 239, 605
 Lam, M. T. 2018, *ApJ*, 868, 33
 Lange, C., Camilo, F., Wex, N., et al. 2001, *MNRAS*, 326, 274
 Lazaridis, K., Wex, N., Jessner, A., et al. 2009, *MNRAS*, 400, 805
 Lower, M. E., Bailes, M., Shannon, R. M., et al. 2020, *MNRAS*, 494, 228
 Miller, M. C., Lamb, F. K., Dittmann, A. J., et al. 2021, *ApJL*, 918, L28
 Morello, V., Barr, E. D., Cooper, S., et al. 2019, *MNRAS*, 483, 3673
 NANOGrav Collaboration, Arzoumanian, Z., Brazier, A., et al. 2015, *ApJ*, 813, 65
 Navarro, J., de Bruyn, A. G., Frail, D. A., Kulkarni, S. R., & Lyne, A. G. 1995, *ApJL*, 455, L55
 Nice, D. J., Sayer, R. W., & Taylor, J. H. 1996, *ApJL*, 466, L87
 Nice, D. J., Splaver, E. M., & Stairs, I. H. 2001, *ApJ*, 549, 516
 Özel, F., & Freire, P. 2016, *ARA&A*, 54, 401
 Parent, E., Sewalls, H., Freire, P. C. C., et al. 2022, *ApJ*, 924, 135
 Pennucci, T. T., Demorest, P. B., & Ransom, S. M. 2014, *ApJ*, 790, 93
 Perera, B. B. P., DeCesar, M. E., Demorest, P. B., et al. 2019, *MNRAS*, 490, 4666
 Riley, T. E., Watts, A. L., Ray, P. S., et al. 2021, *ApJL*, 918, L27
 Schlafly, E. F., & Finkbeiner, D. P. 2011, *ApJ*, 737, 103
 Schlegel, D. J., Finkbeiner, D. P., & Davis, M. 1998, *ApJ*, 500, 525
 Schwab, J., Podsiadlowski, P., & Rappaport, S. 2010, *ApJ*, 719, 722
 Shklovskii, I. S. 1970, *SvA*, 13, 562
 Skrutskie, M. F., Cutri, R. M., Stiening, R., et al. 2006, *AJ*, 131, 1163
 Splaver, E. M., Nice, D. J., Arzoumanian, Z., et al. 2002, *ApJ*, 581, 509
 Stairs, I. H., Thorsett, S. E., & Camilo, F. 1999, *ApJS*, 123, 627
 Stovall, K., Lynch, R. S., Ransom, S. M., et al. 2014, *ApJ*, 791, 67
 Tan, C. M., Bassa, C. G., Cooper, S., et al. 2020, *MNRAS*, 492, 5878
 Tauris, T. M., Kramer, M., Freire, P. C. C., et al. 2017, *ApJ*, 846, 170
 Tauris, T. M., & Savonije, G. J. 1999, *A&A*, 350, 928

- Taylor, J. H. 1992, [RSPTA](#), **341**, 117
- Tremblay, P. E., Bergeron, P., & Gianninas, A. 2011, [ApJ](#), **730**, 128
- Valentina Sosa Fiscella, S., Lam, M. T., Arzoumanian, Z., et al. 2023, [arXiv:2307.13248](#)
- van Straten, W., & Bailes, M. 2011, [PASA](#), **28**, 1
- van Straten, W., Demorest, P., & Osłowski, S. 2012, [AR&T](#), **9**, 237
- Verbiest, J. P. W., & Lorimer, D. R. 2014, [MNRAS](#), **444**, 1859
- Yao, J. M., Manchester, R. N., & Wang, N. 2017, [ApJ](#), **835**, 29
- York, D. G., Adelman, J., John, E. J., et al. 2000, [AJ](#), **120**, 1579
- Zhu, W. W., Stairs, I. H., Demorest, P. B., et al. 2015, [ApJ](#), **809**, 41